processes

MDPI

Article

A Numerical Simulation Study into the Effect of Longitudinal and Transverse Pitch on Deposition of Zhundong Coal Ash on Tube Bundles

Zipeng Guo [1], Jianbo Li [1,*], Yintang Liang [1], Xiaofei Long [1], Xiaofeng Lu [1] and Dongke Zhang [2]

[1] Key Laboratory of Low-Grade Energy Utilization Technologies and Systems, Ministry of Education of China, Chongqing University, Chongqing 400044, China; zipeng.guo@stu.cqu.edu.cn (Z.G.); 202010021043@cqu.edu.cn (Y.L.); 20153257@cqu.edu.cn (X.L.); xfluke@cqu.edu.cn (X.L.)
[2] Centre for Energy (M473), The University of Western Australia, Perth, WA 6009, Australia; dongke.zhang@uwa.edu.au
* Correspondence: jianbo.li@cqu.edu.cn

Abstract: In this paper, the dynamic deposition behavior of Na-enriching Zhundong coal ash on tube bundles with varying longitudinal and transverse pitches was numerically studied. By using a modified critical viscosity model, an improved CFD deposition model has been established and key parameters, including deposit mass and morphology, particle trajectories and impaction and sticking probabilities, as well as the heat flux distribution, have been analyzed. The results show that the ash deposited on tubes in the first row is, respectively, 1.74 and 3.80 times higher than that on the second and third rows, proving that ash deposition in the downstream is lessened. As the longitudinal pitch increased from 1.50 D to 2.50 D, deposit mass in the downstream increased two times, suggesting that an increase in longitudinal pitch would aggravate ash deposition. The effect of transverse pitch, however, with the least deposit propensity at $S_t/D = 1.75$, is non-linear due to the joint effect of adjacent tubes and walls in affecting particle trajectory. In addition, due to the non-uniform distribution of the deposit, heat flux across the tube is the smallest at the stagnation point but becomes six times higher at two sides and the leeward, which makes the thermal damage of these sides to be warranted as a practical concern.

Keywords: ash deposition; CFD modeling; heat flux; particle trajectories; tube bundles; Zhundong coal ash

Citation: Guo, Z.; Li, J.; Liang, Y.; Long, X.; Lu, X.; Zhang, D. A Numerical Simulation Study into the Effect of Longitudinal and Transverse Pitch on Deposition of Zhundong Coal Ash on Tube Bundles. *Processes* **2024**, *12*, 178. https://doi.org/10.3390/pr12010178

Academic Editors: Runxia Cai, Xiwei Ke and Markus Engblom

Received: 21 December 2023
Revised: 6 January 2024
Accepted: 9 January 2024
Published: 12 January 2024

1. Introduction

Ash deposition on heat transfer surfaces in utility boilers has been an intractable problem that needs to be tackled in a practical way [1]. The deposited ash on tube surfaces not only increases the thermal resistance between flue gas and the working fluid, but also brings in potential safety risks such as corrosion and tube explosions [2]. As a consequence, unplanned plant shutdowns have been incurred in certain cases, not to mention the thermal and economic deficiency during operation and maintenance [3–5]. For instance, severe ash deposition on superheaters and re-heaters has been reported during thermal utilization of Zhundong lignite [6,7]. Nonetheless, insights into the dynamic deposition process, including detailed mathematical descriptions and evaluations of the ash transportation process, are still insufficient [8]. Moreover, the effect of tube layouts on the deposition of Zhundong coal ash or the like has not been examined; it has, however, been proven to be an important factor affecting ash deposition [9].

Numerical simulation has provided one means of predicting and analyzing the ash deposition process [10]. By using reasonable numerical solutions, ash deposition models describing the deposition processes can be established [11]. In most cases, the mechanisms of ash deposition, including condensation, thermophoresis and inertial impaction, etc., can

be incorporated, with the impaction, rebounding and sticking behavior of ash particles being evaluated [8,12]. At present, a few deposition models based on critical viscosity [13–15], critical velocity [16,17] and melt fraction, etc. [18,19], have indeed been established. However, the condensation of alkali metals, which has been regarded as an important factor in initiating ash deposition, has often been ignored. In fact, alkali metals are volatile during combustion but will condense subsequently on tube surfaces [20], forming an alkali film on the tube surface [21–23] to facilitate the capture of subsequent ash particles [8,13]. To fill this gap, an improved deposition model considering the condensation of alkali species (mainly Na_2SO_4(g)), thermophoresis and inertia impaction of ash particles on a single tube has therefore been established in our previous study [24].

However, the heat transfer exchangers such as superheaters and re-heaters in practical utility boilers are realized in the form of tube bundles, whose arrangement is also found to be an important factor affecting ash deposition [25,26]. For example, Zheng et al. [27] studied the effect of the longitudinal pitch and transverse pitch of the tube bundle on ash deposition by using CFD dynamic simulation, with the deposition morphology and thermal efficiency characterized and discussed. The results show that the thermal efficiency of the tube bundle decreased from 0.74 to 0.65 when the ratio of the transverse pitch and tube diameter increased from 1.58 to 2.63. Similarly, Manuel et al. [28] conducted a modeling study of a complete staggered heat exchanger to explore the particle deposition behavior of clean and dirty tubes. The cases with fouled tubes presented 7.91% higher deposition rates than what was observed for clean tubes. In addition, Mu et al. [29] proposed a new CFD model to predict the morphological evolution of ash deposits on tube bundles and proved that an elliptical tube could reduce deposition efficiency. Despite these efforts, the dynamic deposition behavior of specific alkali-enriching coal ash particles under typical tube bundle conditions has not been examined, and the heat flux distribution among these tubes as a result of ash deposition has not been examined—both of which are, however, important for the design and operation of boilers burning high-sodium coal.

Zhundong coalfield is the largest coalfield that is being commercially exploited in China. However, severe ash fouling and slagging has incurred in utility boilers during its combustion, which has hindered its clean and efficient utilization. Therefore, as an extension of our previous work [24], this paper presents the latest numerical simulation study into ash deposition on tube bundles with varying longitudinal and transverse pitches, in an effort to comprehend the effect of tube layout on the dynamic deposition behavior of Na-enriching Zhundong coal ash. A modified critical viscosity model has been used to characterize the deposition mass and morphology, the flow field and the particle trajectories over time. In addition, the uniformity of heat flux of the tube bundle as a result of non-uniform ash deposition has been calculated, followed by the specific thermal deviation across the tube being analyzed and discussed. This study could provide an improved understanding of the dynamic deposition behavior of Na-enriching Zhundong coal ash on tube bundles and offer certain references for deposition mitigation during CFB combustion of high-alkali fuels.

2. Physical Models

The physical model of this numerical simulation, as shown in Figure 1, is a set of tube bundles perpendicularly placed in the flue path. Detailed information on ash properties, ash particle size distribution and simulation conditions has been presented in Table 1, which can also be found in our previous publication [24,30,31]. The simulation domain had a height of 100 mm and a length of 500 mm, within which tubes with a diameter (D) of 25 mm are formed into 2 × 3 tube bundles. Tubes in the first row were set 200 mm downstream from the inlet. The longitudinal and transverse pitches were initially set as 2.00 D, i.e., twice the tube diameter, which were then altered to 1.50 D, 1.75 D, 2.25 D and 2.50 D, respectively. With respect to the boundary conditions, the inlet of the domain was set as a velocity boundary, allowing the flue gas and ash particles to be injected, whereas the outlet was set as a pressure boundary and the upper and lower sides were set as wall boundaries.

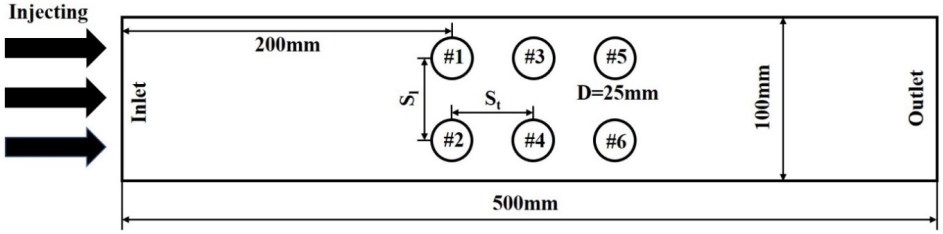

Figure 1. The computational domain for the simulation of ash deposition.

Table 1. A list of ash chemistry and simulation conditions.

Ash Chemistry (wt.%, Dry Basis)									
SiO_2	Al_2O_3	Fe_2O_3	CaO	MgO	TiO_2	SO_3	P_2O_5	K_2O	Na_2O
11.71	6.69	5.93	32.51	7.56	0.39	27.93	0.09	0.44	4.90
Simulation conditions									
Flue gas temperature (K)	Probe temperature (K)		Inlet velocity (m/s)	Concentration of ash (kg/m/s)	Density of ash (kg/m^3)	Porosity of deposit		Thermal conductivity of ash (W/m/k)	
1073	823		15	2.4×10^{-4}	2.5×10^3	0.5		1.89	

3. Deposition Models and Mathematic Solutions

3.1. Discrete Phase Model

In order to calculate the motion trajectory of ash particles accurately, the DPM model is applied to solve the gas–solid two-phase flow. Typically, particle motion is solved in the Lagrange coordinate system, and its momentum equation is expressed as [32]:

$$m_p \frac{d\vec{u}_p}{dt} = m_p \frac{\vec{u} - \vec{u}_p}{\tau_r} + m_p \frac{\vec{g}(\rho_p - \rho)}{\rho_p} + \vec{F} \quad (1)$$

where m_p is the particle mass, $\vec{u}$ is the fluid velocity, $\vec{u}_p$ is the particle velocity, ρ is the fluid density, ρ_p is the particle density, $\vec{F}$ is the additional force and τ_r is the particle relaxation time calculated as below:

$$\tau_r = \frac{\rho_p d_p^2}{18\mu} \frac{24\mu}{C_d \rho d_p \left| \vec{u}_p - \vec{u} \right|} \quad (2)$$

An additional force, the thermophoretic force, is calculated from the expression proposed by Talbot [33], while the temperature gradient between the fluids is considered.

3.2. Deposition Model

The mechanisms of ash deposition, including condensation, thermophoresis and inertial impaction, have been considered in this study. Both inertial impaction and thermophoresis will drive the solid/liquid ash particles to contact the tube surface, while condensation allows for the condensation of inorganic matter in the flue gas to be considered. The deposition rate can therefore be characterized as below [12]:

$$\frac{dM_d}{dt} = Q_{impact} P_{stick} + I_v \quad (3)$$

where M_d is the deposit mass, Q_{impact} is the mass flow rate of impacting particles, P_{stick} is their corresponding sticking probability and I_v is the mass flux of alkali vapor condensation,

with Na_2SO_4(g) being the condensable component calculated with the formula proposed by Jokiniemi [34]:

$$I_v = Sh(T_g)\frac{\left[D_v(T_g)D_v(T_s)\right]^{\frac{1}{2}}}{D_h R_g}\left[\frac{p_v(T_g)}{T_g} - \frac{p_{v,s}(T_s)}{T_s}\right] \tag{4}$$

$$Sh(T_g) = 0.023Re^{0.8}Sc(T_g)^{0.4} \tag{5}$$

$$Sc(T_g) = \frac{\mu_g}{\left[\rho_g D_v(T_g)\right]} \tag{6}$$

where $Sh(T_g)$ is the Sherwood number, $Sc(T_g)$ is the Schmidt number, Re is the Reynolds number, $D_v(T)$ is the vapor diffusivity at vapor temperature T_g or surface temperature T_s, $p_v(T_g)$ is the vapor patrial pressure, $p_{v,s}(T_s)$ is the saturated vapor pressure, D_h is the channel hydraulic diameter and R_g is the specific gas constant.

For the sticking probability P_{stick}, a modified critical viscosity model expressed as follows is adopted:

$$p_{stick} = \left\{\underbrace{p_p(T_p)}_{[1]} + \underbrace{\left[1 - p_p(T_p)\right]p_S(T_S)}_{[2]}\right\}\underbrace{(1 + SI_v)}_{[3]} \tag{7}$$

$$P_{stick} = \begin{cases} \frac{\eta_{ref}}{\eta} & \eta > \eta_{ref} \\ 1 & \eta \le \eta_{ref} \end{cases} \tag{8}$$

In Equation (7), the first and second terms represent the deposition of sticky particles on the surface and the deposition of non-sticky particles on the sticky surface, respectively. $p_p(T_p)$ and $p_s(T_s)$ are the sticking probability of the particles and the deposition surface, which can be calculated using the critical viscosity formula Equation [8,13,35,36].

As for Equation (8), η is the viscosity of the particle, calculated using the S^2 model [37] proposed by the British Coal Utilization Research Association based on the particle temperature and the particle composition:

$$S = \frac{\mathrm{SiO_2}}{\mathrm{SiO_2}+\mathrm{Al_2O_3}+\mathrm{Fe_2O_3}+\mathrm{CaO}+\mathrm{MgO}} \tag{9}$$

$$\lg\eta = 4.468\left(\frac{S}{100}\right)^2 + 1.265\left(\frac{10^4}{T}\right) - 7.44 \tag{10}$$

where S is the percentage of silica (SiO_2). Each compound in Equation (9) refers to the normalized weight percentage of each component in the ash. Based on the particle chemistry for viscosity calculation (Equations (9) and (10)), the characteristics of high-alkali fuel ash formation and melting characteristics could be reflected. η_{ref} is the critical viscosity, calculated using the empirical formula based on particle kinetic energy in accordance with Kleinhans [14]:

$$\eta_{\text{ref}} = 5 \cdot 10^{-12} \cdot \left(\frac{1}{12}\pi d_p^3 \rho_p u_p^2\right)^{-1.78} \tag{11}$$

The third term represents the promoting effect of the alkali film formed by the condensation of alkali vapor (Na_2SO_4) on the formation of ash deposits. The deposition rate coefficient, S, is provided by Tomeczek et al. [21] and is taken as S = 62 $(kg/m^2s)^{-1}$, and the alkali vapor concentration is determined using the calculation of Ji et al. [38], which is 1.1 ppm at the furnace outlet.

3.3. Dynamic Mesh

In order to simulate the dynamic growth process of ash deposition more accurately, the dynamic mesh method was used to characterize the change of deposition morphology

over time [19,39]. When a particle is determined to be deposited on a surface, the particle mass is recorded in the User-Defined Memory (UDM) for that mesh face, increasing per mesh face by:

$$\Delta\delta_j = \frac{\Delta m_j}{\rho_p(1-\varepsilon)A_j} \tag{12}$$

$$\Delta\delta_j = \frac{\Delta\delta_{j-3} + 2\Delta\delta_{j-2} + 3\Delta\delta_{j-1} + 4\Delta\delta_j + 3\Delta\delta_{j+1} + 2\Delta\delta_{j+2} + \Delta\delta_{j+3}}{16} \tag{13}$$

On the j mesh surface in a time step, $\Delta\delta_j$ is the growth height, Δm_j is the deposition mass, A_j is the mesh area, ρ_p is the particle density and ε is the porosity, which is taken as 0.5 [18]. In order to prevent the phenomenon of "negative grid" between adjacent meshes, the growth height is homogenized, as shown in Equation (7), and the weighted average is applied to $\Delta\delta_j$.

The displacements of the faces are transferred to the displacements of the nodes to apply the dynamic mesh method, and the displacement of each node is determined by the adjacent faces:

$$\Delta M_j = \frac{\Delta\delta_j + \Delta\delta_{j+1}}{2} \tag{14}$$

For the update direction of the node, the windward side grows along the horizontal direction as most particles hit the deposition surface horizontally, while the leeward side grows along the radial direction since ash deposition is largely induced by the impingement of vortices.

3.4. Solution Procedure

Figure 2 highlights the flow chart of the simulation process. When ash particles impact and stick to the surface, their data will be recorded and deposition will be generated. As for the tube bundle, the rebounded particles may still impact or deposit on other tubes in the process of subsequent movement, and particles that do not impact in the first row are also likely to impact a tube in the second and third rows.

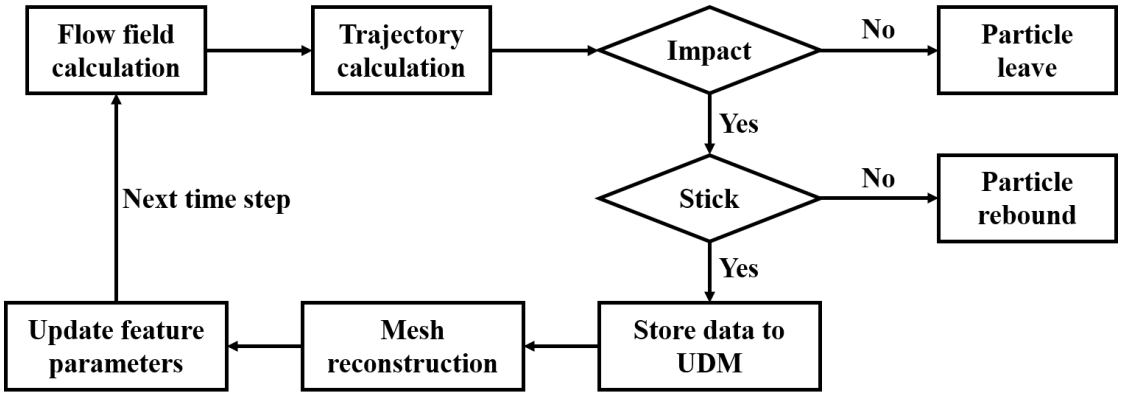

Figure 2. A logic flow chart of numerical solution of the particle deposition process.

The CFD simulation software used is ANSYS-fluent 2021. The k-ω model and the wall function were used for turbulence calculation, and the P1 model was used for radiation heat transfer. The DPM model was used to calculate particle trajectories and consider the gas–solid phase interaction, as well as heat transfer. The self-compiling subroutines were compiled and loaded into corresponding modules with the User-Defined Function (UDF). In addition, the simulation time step was set to 0.01 s. In order to reduce the calculation time, the asynchronous growth method with an update cycle of 1s was adopted. The accuracy of this method has been widely recognized [19,27,39] and verified in our previous work [24].

3.5. Mesh Independence Analysis

Figure 3 gives the mesh settings of the computational domain. In order to ensure the smooth application of the dynamic mesh program, the triangular mesh was used for division, and the mesh was refined at the surface of each tube to ensure the accuracy of the flow field and particle trajectory near the surface. Three mesh systems were generated to verify the grid independence, and the meshes were increased at a rate of 1.141 times, with the mesh sizes being 0.2 mm, 0.3 mm, 0.4 mm at the near-surface and the overall number of meshes being 62,724, 127,352, 226,809. After calculating for 10 min, the temperatures of ten equally spaced cross-sections with an interval of 50 mm were extracted for comparison. The results in Figure 4 showed that an increase in the mesh cell to 127,352 and 226,809 would give identical results. Therefore, a mesh system of 127,352 cells has been applied.

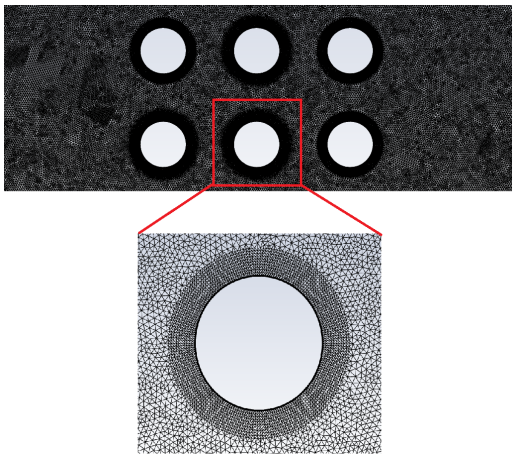

Figure 3. The mesh of the computational domain.

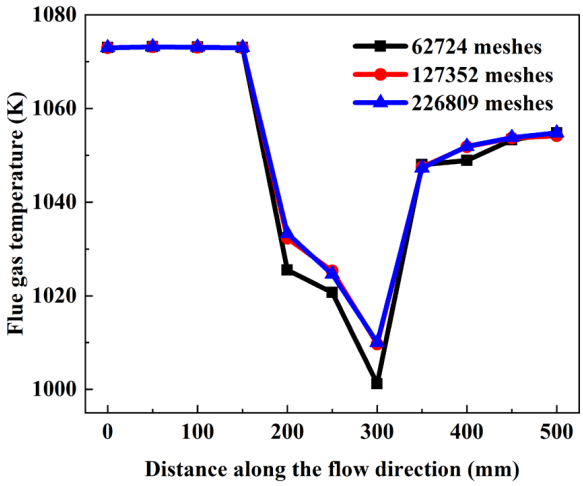

Figure 4. The mesh independence analysis.

3.6. Model Validation

The developed simulation method was validated against the experimental data by simulating the formation of deposits on a single tube, which has been verified in our previous work [24]. Briefly, the deposit as simulated presents a cone-shaped structure to the windward of the probe, and its thickness at the stagnation point reaches to 3.4 mm within a duration of 6 h. This is comparable to the experimental result of 3.0 mm with the same experimental setup (Figure 5) [30], suggesting that the current model is able to simulate the deposition of Zhundong coal ash on single or multiple tubes. Furthermore, the size distribution of deposited ash on the windward and leeward are also in accordance with

the experimental analysis [40]. These confirm a good agreement between the simulation results and experimental data, enabling the effect of tube layouts on ash deposition to be investigated [27].

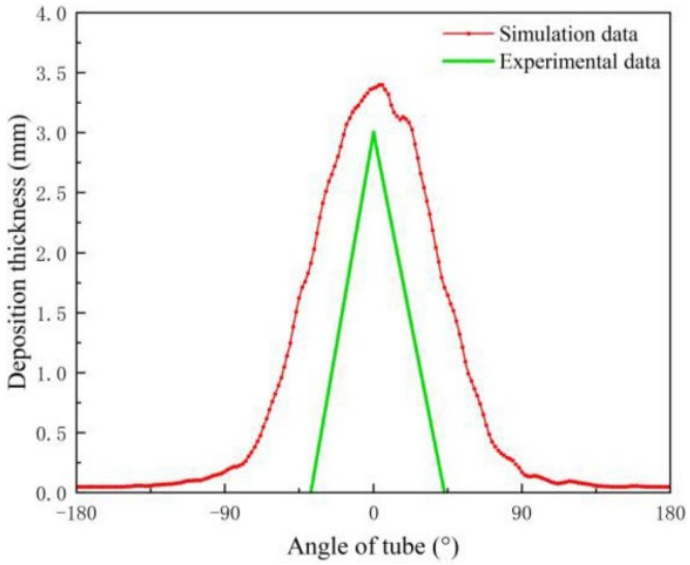

Figure 5. Simulation result versus experimental data (stagnation point to the windward being 0°) [24].

4. Results and Discussion

4.1. Deposit Mass and Morphology

Figure 6 presents the simulated deposit morphology and its thickness on the 2 × 3 tube bundles in the domain using the current deposition model. It is evident that inevitable deposits have been accumulated on the tubes after 6 h. These deposits are mainly formed on the windward of the tubes, confirming the role of inertial impaction to be dominant for deposit accumulation [12]. Moreover, certain deposits on the leeward side are also observed, particularly on the first and second rows. This is attributed to the eddy effect [9] and the presence of rebounding particles on the windward side of the back rows [21,41], which will be discussed in Section 4.2. To be more specific, as shown in Figure 6b, the thickness of the deposit at the stagnant point of the tube in the first row (i.e., tubes #1 and #2) is ca. 7.2 mm, which decreases to 3.2 mm and 2.0 mm on tubes in the second (tubes #3 and #4) and third rows (tubes #5 and #6). This confirms that ash deposition on tubes in the first row is the worst but will be lessened on subsequent rows, consistent with the results reported in Refs. [21,41–43]. As for the leeward side, a deposit with a thickness of ca. 0.50–1.0 mm has been accumulated on tubes in the first and second rows but not in the third rows. As a consequence, the weight of deposits on the tubes in the first row, being 0.186 kg/m (Table 2), is 1.74 and 3.80 times higher than the second and third rows, respectively.

Table 2. Partial simulation results for tubes among different rows.

	Impaction Probability	Sticking Probability	Mean Size of Impacting Particles (μm)	Deposit Mass (kg/m)
1st row	0.3486	0.0538	85.2	0.186
2nd row	0.1758	0.0163	89.1	0.107
3rd row	0.1281	0.0106	89.4	0.049
Single [24]	0.2191	0.0717	81.2	0.085

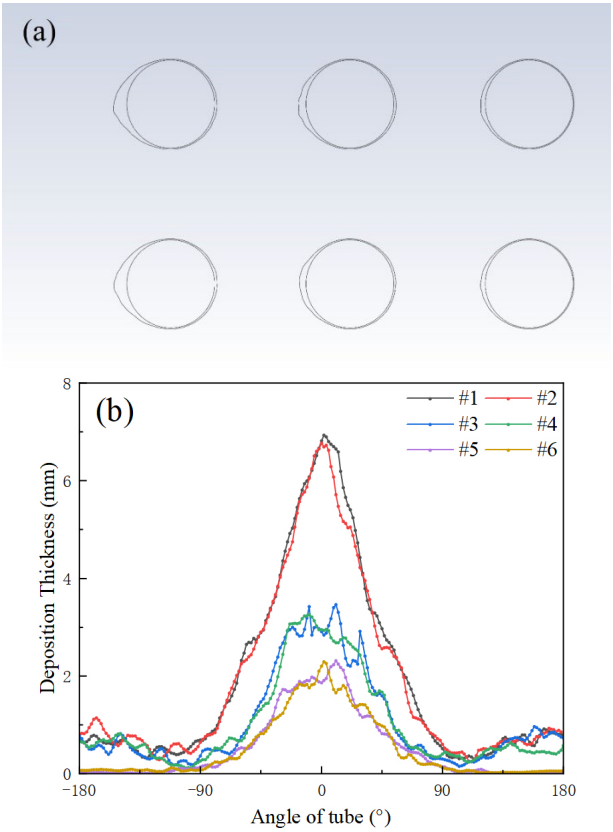

Figure 6. Simulation results from the current deposition model (**a**) deposit morphology and (**b**) deposit thickness on the 2 × 3 tube bundles.

To reveal the reasons for the deposit formation on tubes in different rows, the probabilities of particle impaction and particle sticking, as well as the mean size of the impacting particles, have been summarized and listed in Table 2. Herein, the impaction probability defines the ratio of impaction particles to the total particles, and the sticking probability means the ratio of sticking particles to impaction particles. As shown in Table 2, the probability of particles impacting on tubes in the first row is 0.3486, which then decreases to 0.1758 and 0.1281 for tubes in the second and third rows. This is because the tubes in the first row act as a barrier, and fewer ash particles would impact on the subsequent tubes due to a decrease in particle numbers and the variation in particle trajectories [41]. As for the sticking probability, it is 0.0538 for tubes in the first row but becomes 0.0163 and 0.0106 for tubes in the subsequent rows. This is attributed to either the chemistry of particles or the particle size. For the first reason, ash particles enriching in Na and Ca of a smaller size tend to deposit on the tubes in the first row instead of rebounding [41]. However, particles with larger sizes and higher kinetic energies prefer to rebound upon impacting on the probe surface [24]. This has also been confirmed by the mean size of the impacting particles, which increases from 85.2 μm in the first row to 89.4 μm in the third row, since particles with finer sizes and higher Na/Ca content might have been deposited on previous tubes.

Compared these results with those on a single tube in the domain [24], the probability of particles impacting on tubes in the first row, being 0.3486, is 1.59 times higher than that on the single tube, resulting in a deposit mass 2.19 times higher than the single tube case. This means that more ash particles have impacted and deposited on the tubes, particularly on tubes in the first row. Since the injection concentration of the ash particles between these two simulations is the same, the variation in impaction probability could be attributed to either the extra ash particles from adjacent tube surfaces or the wall boundaries as a result of rebounding. This also highlights the importance of particle trajectories in Section 4.2 being examined.

4.2. Dynamic Particle Trajectories

To comprehend the dynamic deposition behavior of ash particles on tube bundles, the transient trajectories of ash particles in the domain subjected to a deposition time of 2, 4 and 6 h have been illustrated in Figure 7. It can be seen that the trajectories of ash particles varied dynamically with physical spaces and time. As a representative, at a deposition time of 2 h, certain ash particles have deposited on the tubes, resulting in a non-circular deposit "surface" embracing the subsequent ash particles. In the first row in particular, a cone-shaped deposit on tube #1 (and also #2) has been formed due to the impaction and sticking of ash particles. Since the sticking probability of the impacting ash particles is less than 0.1, most ash particles would leave the tube surface after impaction. The rebounded ash particles, depending on their contact angles [10], would have different directions. For those ash particles impacting on tube #1, for example, they may rebound upward and move to the solid boundary of the domain. Since there is no heat and mass transfer across the boundary, these ash particles would firstly impact on the wall but then rebound from it again, with a portion of ash particles impacting on the tube once more, as evidenced in Figure 7a. Alternatively, these ash particles, after impacting on tube #1, could move downward and across the centerline of the domain to possibly impact on tube #2. A similar analysis of the behavior of ash particles could also be applied to tube #2. These support why the impaction probability of ash particles on the tubes in the first row is higher than the ash deposition on a single tube [21,41]. Moreover, differing from the impacting ash particles in the first row, the ash particles impacting on the second and third rows are not directly impacting on the stagnant point of the tube. Instead, they impact on the two sides around the stagnant point, resulting in a deposit with a broader width and bimodal distribution (shown in Figure 6). This is because the ash particles injected into the domain are hindered by the tubes in the front rows, and only those particles twisting their directions upward or downward could be able to potentially impact on the tubes in subsequent rows. In addition, it is observable that a large number of ash particles have impacted on the windward side of the back row tubes, resulting in an obvious deposition on the leeward side [26]. As for the tubes in the third row (Figure 7d), the deposition is only caused by an eddy current effect due to the absence of rebound particles, resulting in less particles being deposited.

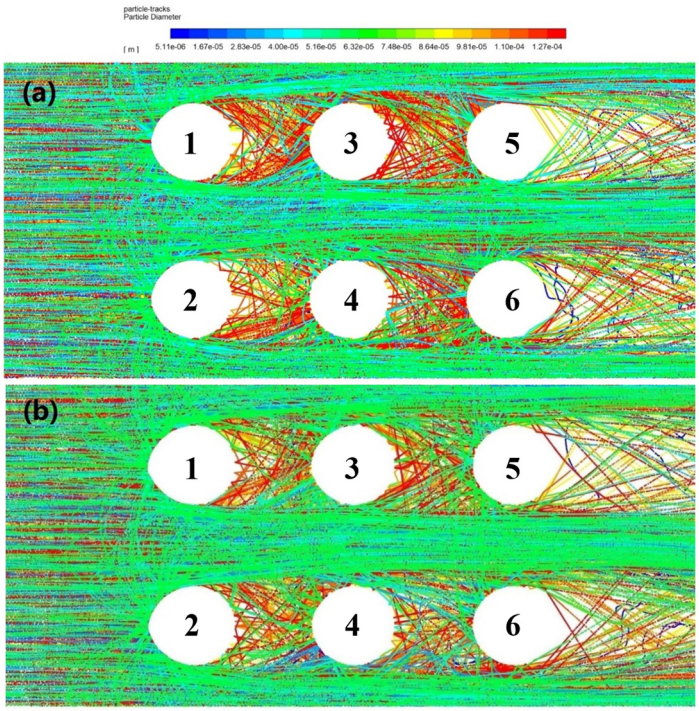

Figure 7. *Cont.*

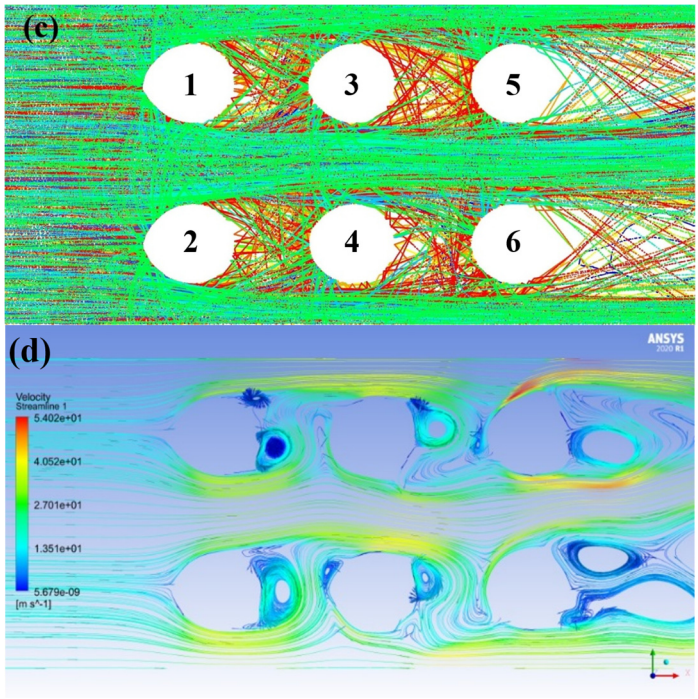

Figure 7. Trajectories of ash particles at the deposition time of (**a**) 2, (**b**) 4 and (**c**) 6 h, and (**d**) the velocity streamline of the flue gas in the domain.

As deposition proceeds to 4 and 6 h, as shown in Figure 7b,c, one can tell that the cone-shaped deposit increases its thickness, particularly for the deposits on tubes #1 and #2 in the first row. This can be proved by the deposit thickness on tube #1 (and tube #2) as a function of time shown in Figure 8. The thickness of the deposit at the stagnant point on tube #1 increases from 2.0 mm to 7.2 mm as the deposition time proceeds from 1.5 to 6.0 h (shown in Figure 8). In this case, the rebounding direction of the impacting particles would be altered, which in turn affects the subsequent impacting and sticking behavior of the ash particles. For instance, the ash particles tend to rebound to the downward zone upon impaction as the deposit accumulates. Nonetheless, such a trend still warrants further and quantitative investigation, which will be a continuous work for this study.

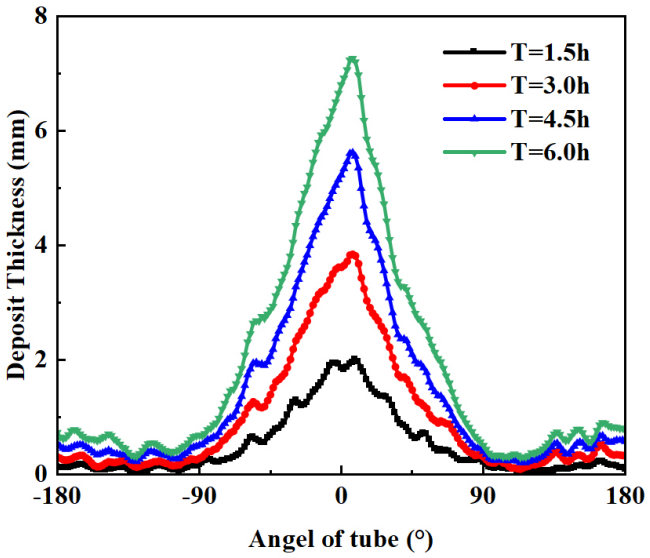

Figure 8. Thickness of the deposit on tube #1 as a function of time.

4.3. Effect of Tube Layouts

The effect of tube layouts, i.e., the longitudinal pitch and transverse pitch, on the characteristics of ash deposits on the tube bundle was also studied, and the results are illustrated in Figures 9–11. Figure 9 presents the effect of tube layout on the weight of deposits that accumulated on the tube. As shown in Figure 9a, the deposited mass on tube #1 maintains at ca. 0.18 kg/m at different longitudinal pitches and seems to be independent of the longitudinal pitch. Meanwhile, the deposit on tube #3 in the second row increases its weight from 0.04 kg/m to 0.11 kg/m as the longitudinal pitch increases from 1.50 D to 2.00 D, but then decreases gradually to 0.08 kg/m as the longitudinal pitch further increases to 2.50 D. As for the deposit on tube #5 in the third row, its mass increases from 0.02 kg/m to 0.04 kg/m as the longitudinal pitch increases to 2.00 D but then maintains at this level regardless of the increase in the longitudinal pitch.

For the effect of transverse pitch, as shown in Figure 9b, a deposit with a weight of 0.22 kg/m accumulates on tube #1 at a transverse pitch of 1.50 D. This, however, becomes ca. 0.18 kg/m at a transverse pitch of 1.75–2.25 D, but then increases again to 0.22 kg/m as the transverse pitch increases to 2.50 D. Likewise, the deposit on tube #3 is 0.11 kg/m at a transverse pitch of 1.50 D, which maintains relatively the same at this level as the transverse pitch increases to 2.25 D but declines to 0.06 kg/m at a transverse pitch of 2.50 D. A similar trend is also observed for tube #5 in the third row.

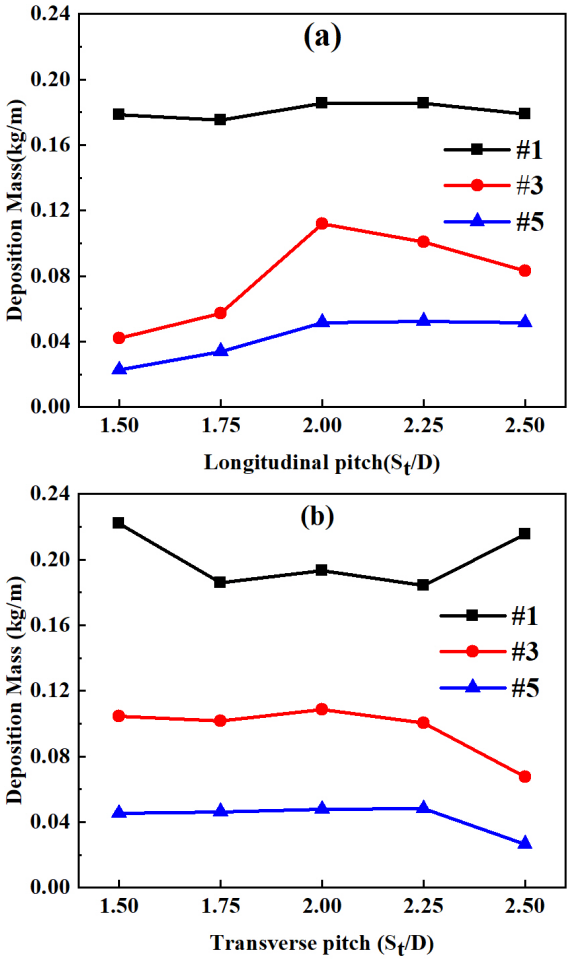

Figure 9. Weight of deposits on tubes as a function of (**a**) longitudinal pitch and (**b**) transverse pitch.

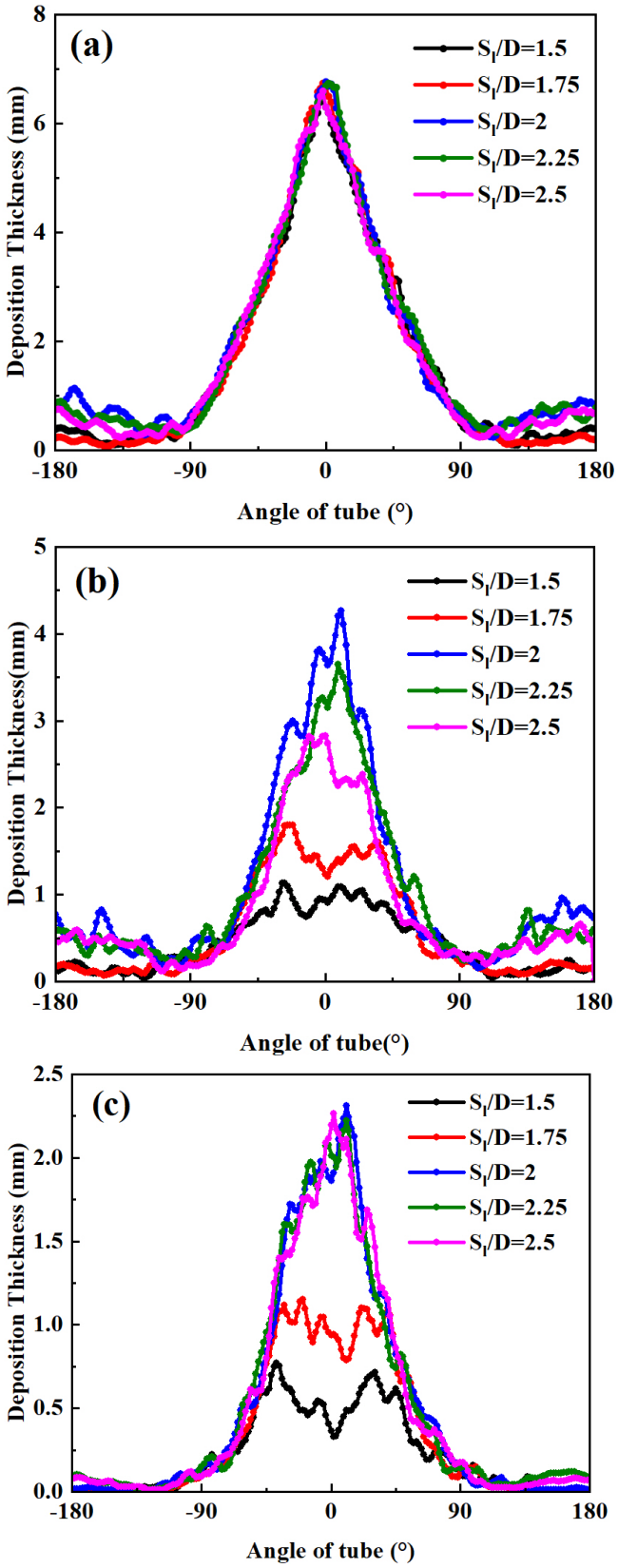

Figure 10. Thickness of deposits on tube (**a**) #1, (**b**) #3 and (**c**) #5 at varying longitudinal pitches.

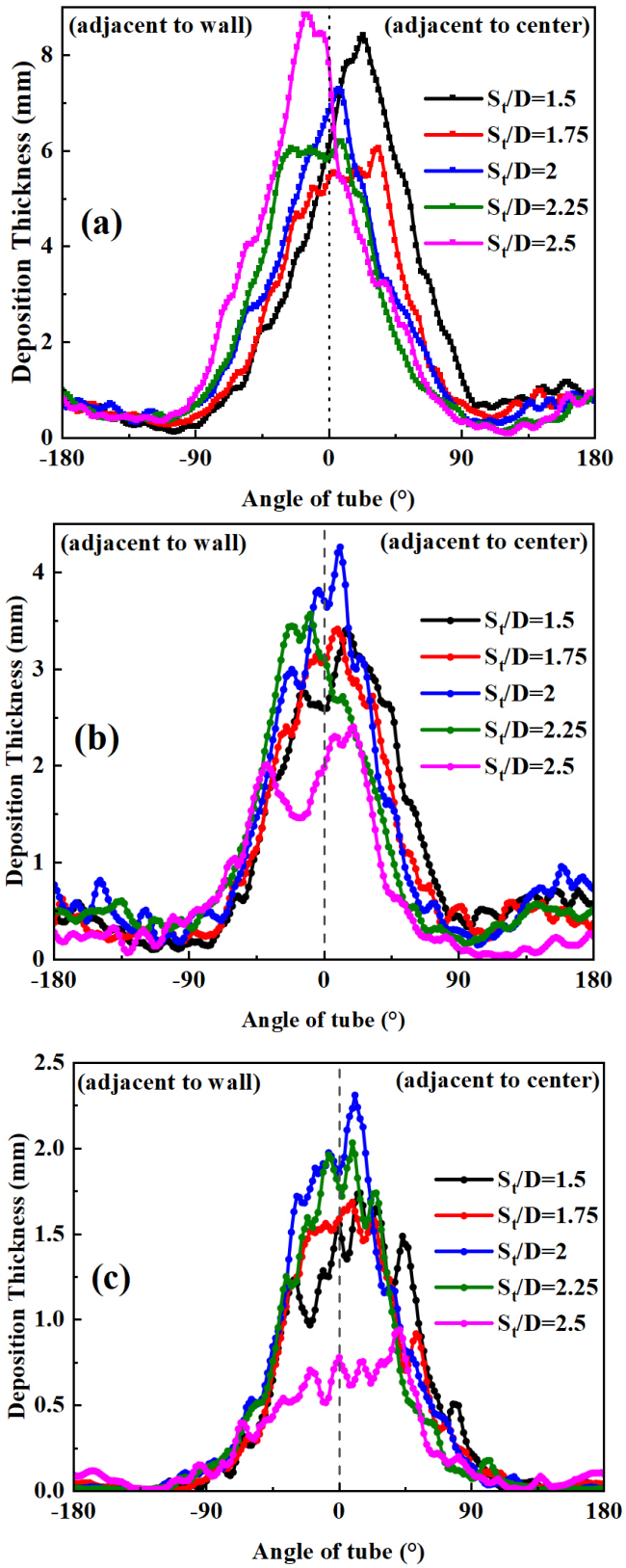

Figure 11. Thickness of deposits on tube (**a**) #1, (**b**) #3 and (**c**) #5 at varying transverse pitches.

To further investigate the role of longitudinal pitch and transverse pitch in ash deposition, the thickness of deposits on tube surfaces are comprehensively provided. Figure 10 gives the thickness of the deposit subjecting to different tube layouts. For the tube bundle with a transverse pitch of 2.00 D, the thickness of the deposit at the stagnant point on tube

#1 in the first row maintains basically at 7.2 mm and is independent of the longitudinal pitch in the range of 1.50–2.50 D. This implies that the gas–solid flow arriving at the tube in the first row is not affected by the subsequent tubes no matter the layout [28]. This also confirms the repeatability of this simulation work. At the leeward side of the tube, however, the thickness of the deposit increases initially to a certain degree as the longitudinal pitch increases from 1.50 D to 2.00 D but then decreases as the longitudinal pitch further increases to 2.50 D. A similar trend is also found on the windward side of the second row, where the highest deposit thickness of 4.3 mm is obtained at a longitudinal pitch of 2.00 D. This means that the formation of the ash deposit on tubes in the second row is the worst at a longitudinal pitch of 2.00 D, which therefore could be mitigated by increasing or decreasing the longitudinal pitch. This is mainly attributed to the particle trajectories as discussed above. Briefly, at a pitch of 2.00 D, more particles could pass through the first rows and impact on tubes in the second row, thereby increasing the deposition of particles on the leeward side of the first row. Likewise, the thickness of the deposit at the stagnant point on tubes in the third row increases from 0.5 mm to 1.0 mm and 2.25 mm as the longitudinal pitch increases from 1.50 D to 2.00 D, which then maintains at this level as the longitudinal pitch increases to 2.50 D. This indicates that increased longitudinal pitch could aggravate ash deposition, which might be attributed to the increased flight time of particles before they impact the tube [27].

Figure 11 presents the thickness of the deposits on these tubes at a longitudinal pitch of 2.00 D and transverse pitches of 1.50–2.50 D. For deposits on tubes in the first row (Figure 11a), it is seen that a maximum thickness of the deposit has been formed at a transverse pitch of 2.50 D; this is followed by those with a transverse pitch of 1.50 D, 2.00 D, 2.25 D and 1.75 D, respectively, showing a non-linear relationship with transverse pitch. Moreover, it is also observable that the centerlines of the deposits are not always at the stagnant point of the tube. For instance, the centerline of the deposit shifts to the center of the domain at a smaller transverse pitch of 1.50 D, but moves to the wall (boundary) at a larger transverse pitch of 2.50 D. This is attributed to the effect of the wall and the adjacent tube in changing particles' trajectories, as has been discussed comprehensively in Section 4.2. With a narrower transverse pitch, ash particles that rebound from one tube would have more chance of impacting and depositing on its adjacent tube, resulting in more ash particles accumulating on this side and consequently a shift in the deposit centerline towards the center. Similarly, tubes with a higher transverse pitch are closer to the walls, resulting in more ash particles depositing on this side and shifting the deposit centerline to the wall.

For the deposits on tubes in the second and third rows, they become even more complicated, with two main humps and a number of minor humps being observed at the windward side of the tube. Within the ranges examined, a maximum thickness of 4.1 mm is obtained on tube #3 at a transverse pitch of 2.00 D and a minimum thickness of 2.2 mm at a transverse pitch of 2.50 D, with the remaining deposit thickness falling into this region. Similar findings are also observed for deposits on tubes in the third row, within a decreased deposit thickness of 0.9–2.2 mm. This implies the joint effect of the wall and the adjacent tube in particle trajectories and deposition.

To analyze separately the role of wall boundaries and the adjacent tubes in affecting ash deposition, the deposit is divided into two parts in accordance with the horizontal centerline of the tube. Figure 12 illustrates the weight of ash deposit that accumulated on the 1/2-tube either close to the wall or close to the adjacent tube. It is clear that the deposits accumulated on surfaces adjacent to the center decrease with increasing transverse pitch. Typically, the weight of deposit on 1/2-tube #1 in the first row decreases from 0.15 kg/m to ca. 0.08 kg/m as the transverse pitch increases from 1.50 D to 2.25 D and 2.50 D. Similarly, the deposit on 1/2-tubes in the second and third rows decreases, respectively, to 0.03 and 0.01 kg/m as the transverse pitch increase to 2.50 D. The weight of deposit on 1/2-tube #1 in the first row decreases 47% as the transverse pitch increases from 1.50 D to 2.50 D, whereas the deposit on 1/2-tube #3 and 1/2-tube #5 in the second and third rows decreases,

respectively, 55% and 67%. This is because an increase in the transverse pitch would decrease the chances for the rebounding ash particles from the adjacent tube to impact on the surface. Similar findings were also found in [27]. This also explains why the deposit mass on the tube in this study overweighs that on a single tube in the domain [24].

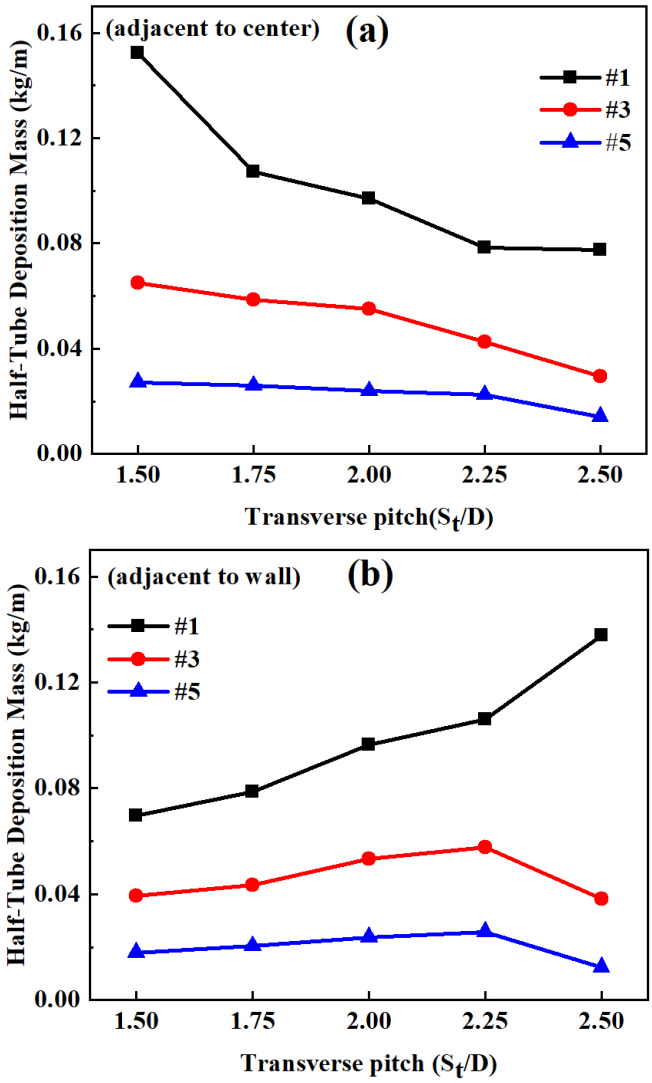

Figure 12. Weight of the deposit on 1/2-tube surface adjacent to (**a**) center and (**b**) wall.

As for the effect of wall boundaries, as shown in Figure 12b, the weight of deposit on this side increases with increasing transverse pitch. Representatively, the weight of deposit on 1/2-tube #1 facing the wall is 0.07 kg/m at a transverse pitch of 1.50 D, which is doubled at a transverse pitch of 2.50 D, being 0.14 kg/m, an increase of 50%. This is because the ash particles that impact on the wall would again change their direction and then impact on the tube, as elucidated in Figure 6 and other literature reports [21,41]. Likewise, the deposit on 1/2-tube #3 and 1/2-tube #5 increases its weight as the transverse pitch increases from 1.50 D to 2.25 D but decreases its weight as the transverse pitch further increases to 2.50 D. A possible explanation is that the distance between tubes and boundary is too close to promote enough space for gas–solid flow, consequently decreasing the possibility for ashes to deposit on this side. Based on the analysis above, it could be concluded that an optimal transverse pitch could be obtained (S_t/D = 1.75 in this work) during design, considering the joint effect of adjacent tube and wall boundaries in ash deposition.

4.4. Heat Flux and Temperature Uniformity

The formation of the ash deposits on tube bundles also affects the heat transfer between the steam inside the tube and the flue gas outside by acting as an additional thermal resistance [8]. The surface temperature of the deposit would therefore be increased, as widely discussed in the literature [12,19,27]. Herein, the surface temperatures of the deposits on tubes #1, #3 and #5 as a function of time are given in Figure 13. It is seen that the mean surface temperature of the deposit on tube #1 increases gradually from the initial temperature of 826 K to 980 K as deposition time proceeds to 6 h. Similarly, the mean surface temperatures of the deposits on tube #3 and tube #5 are also found to increase to 960 K and 925 K within the simulation time. This is attributed to the discrepancy in deposit thickness, since the deposit weight on tube #1 is the highest, followed by those on tubes #3 and #5 in the second and third rows. An increase in the surface temperature would firstly aggravate the sintering and fusion propensity of the deposit, which would in turn accelerate the deposition of coal ash on the tubes and increase the thermal resistance between the flue gas and the steam. Moreover, sintering strength within the deposit would also be increased, thereby decreasing the shedding of the deposit using the existing soot-blowing technique.

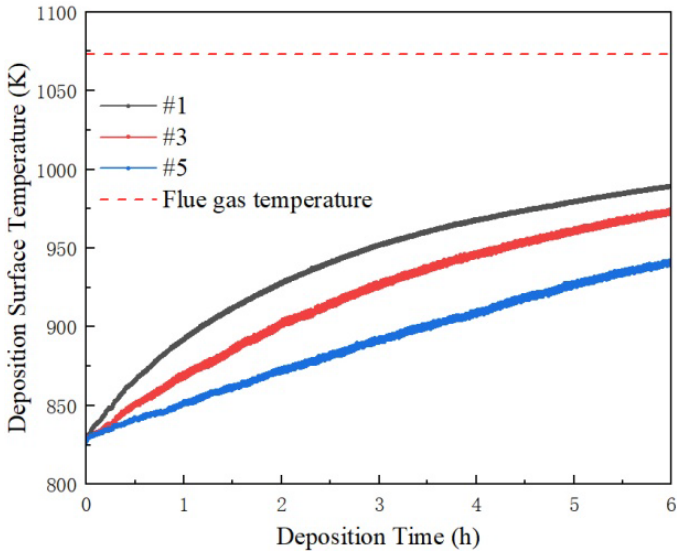

Figure 13. Surface temperatures of the deposits on tubes #1, #3 and #5 as a function of time.

Nonetheless, analysis into the surface temperature, as above, as well as heat flux, is mostly based on their averaged value [12,44], which to a large degree underestimates the non-uniform distribution of ash deposits in affecting heat flux and temperature distribution. The distribution of heat flux across the tube is therefore further investigated to comprehend how heat flux varies with deposit accumulation.

A steady-state heat transfer simulation based on a physical model of the fouled tubes has been conducted, and the distribution of heat flux and wall temperature at the tube cross-sections can be seen in Figure 14. One can find that the heat flux between the steam and the flue gas varies with the tube's angle. This is due to the non-uniform distribution of the ash deposits as shown in Figure 6. Typically, heat flux at the stagnant point of tube #1, with a value of 10,000 W/m^2, is the lowest among them. This is consistent with its highest deposit thickness at the stagnant point, confirming the role of the deposit in adversely affecting heat transfer. The heat flux then increases gradually as the tube position leaves the stagnant point, reaching a highest heat flux of 45,000–60,000 W/m^2 at the two sides of the tube. This is attributed to the low deposit accumulation and high gas flow rate at these positions. The heat flux then decreases gradually to ca. 40,000 W/m^2 and increases afterwards to 50,000–60,000 W/m^2 at the leeward side of the tube. The maximum deviation

of the heat flux at the tube cross-sections is up to six times, highlighting the role of deposit distribution and the gas flow field in affecting heat transfer.

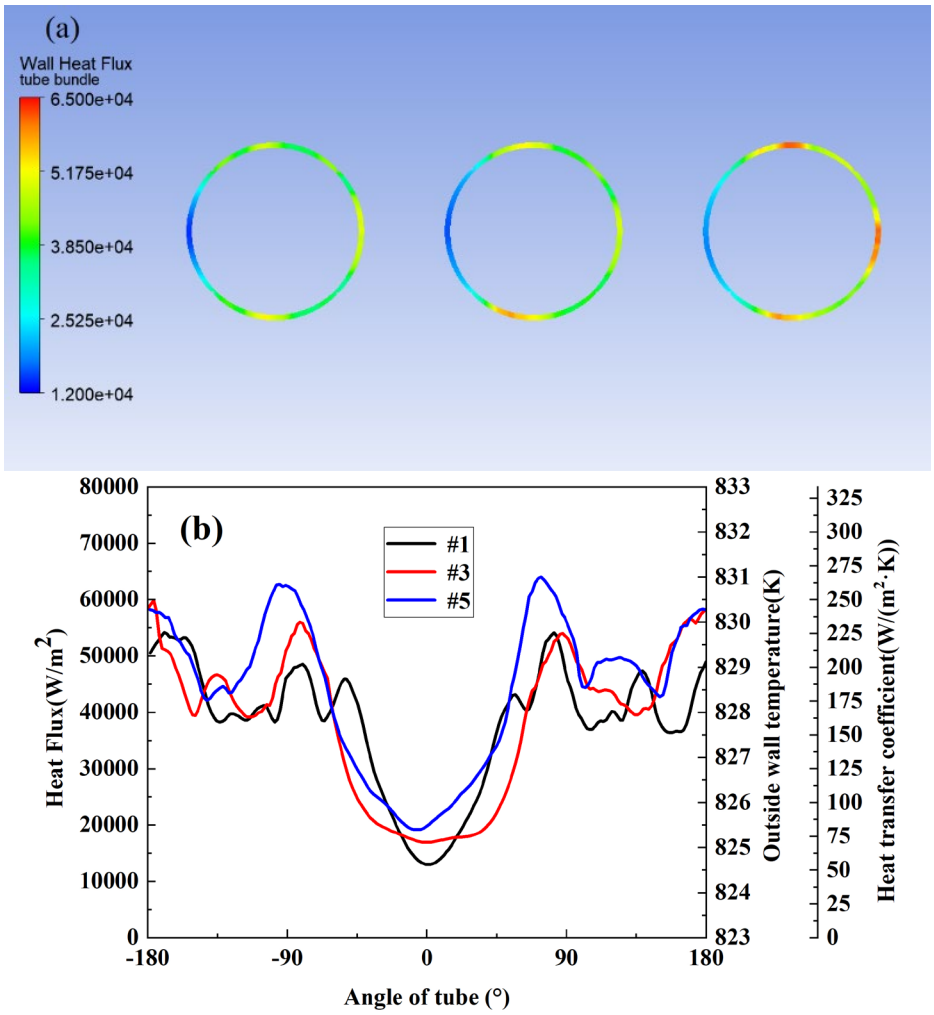

Figure 14. Distribution of (**a**) heat flux and (**b**) wall temperature and heat transfer coefficient at the tube cross-sections at deposition time of 6 h.

Analysis into the distribution of heat flux across the tube circularly also allows for the temperature distribution of the tube (outer) surface to be examined. The lowest tube surface temperature of 824.5 K is observed at the stagnant point of tube #1 due to its lowest heat flux, whereas a highest tube surface temperature of 831 K occurs at the two sides of tube #5 because of its highest heat flux. This means that the worst condition for the safety of steam tubes occurs at tube #5 in the third row, rather than tubes in the first and second rows. As shown in Figure 14b, due to non-uniform distribution of the deposits, the lowest heat transfer coefficient of 52.24 W/(m^2·K) was observed at the stagnation point of tube #1 but the highest heat transfer coefficient of 264.46 W/(m^2·K) was found at both sides of tube # 5.

Noteworthily, the thickness of the tube is set as 2 mm, which limits the tube surface to an acceptable temperature of 831 K [24]. In industrial practice, with an even higher thickness of 6.0–8.0 mm, the maximum temperature of the tube surface could be increased. Moreover, in order to maintain the rated output in industrial boilers, more fuel and a higher flue gas temperature are required [7]. These would inevitably raise the risks of tube explosions as a result of overheating. Attention should thus be paid not only to the deposit characteristics but also to the safety of the tubes, particularly tubes installed downstream where sufficient deposits are not covered. Moreover, in industrial practice, designers should design the tube bundles with appropriate tube distances, and the accumulation of

deposition in the first row and at the pipeline station need to be focused on to strengthen the blowing in this area.

5. Conclusions

In this paper, the dynamic deposition behavior of Zhundong coal ash on tube bundles subjected to different tube layouts has been studied using a modified deposition model. The key parameters, including deposit mass, deposit morphology, particle trajectories and particle impaction/sticking probabilities, as well as the heat flux uniformity, have been analyzed for an improved understanding of the deposition process. The results show that the deposit mass on the first row is, respectively, 1.74 and 3.80 times higher than the second and third rows. This proves that ash deposition on tubes in the downstream are lessened and also highlights the importance of finer Na/Ca-enriching ash particles in initiating ash deposition. When the longitudinal pitch increases from 1.50 D to 2.50 D, the deposit mass on the first row is almost unchanged, while that in the downstream increases two times, suggesting that an increase in the tube's longitudinal pitch would increase the propensity for ash deposition. Moreover, as the transverse pitch increases from 1.50 D to 2.50 D, the centerline of the deposit on the first row shifts to the wall or the adjacent tube due to the joint effect of adjacent tubes and walls in affecting particle trajectories, resulting in the least deposit mass at a transverse pitch of 1.75. In addition, heat flux at the stagnation point of the tubes is found to be the smallest, whereas those on both sides and the leeward side are six times higher than the windward. This leads to the occurrence of the highest tube temperature at both sides, bringing the thermal damage of these areas to be warranted as a concern as a result of the non-uniform deposition of the ash studied.

Author Contributions: Conceptualization, J.L. and D.Z.; methodology, Z.G., J.L. and X.L. (Xiaofeng Lu); software, Y.L.; validation, Z.G., X.L. (Xiaofei Long) and Y.L.; formal analysis, Z.G.; investigation, Z.G. and Y.L.; resources, X.L. (Xiaofeng Lu); data curation, Z.G.; writing—original draft preparation, Z.G. and Y.L.; writing—review and editing, J.L. and D.Z.; visualization, Z.G. and Y.L.; supervision, J.L. and X.L. (Xiaofeng Lu); project administration, J.L.; funding acquisition, J.L. All authors have read and agreed to the published version of the manuscript.

Funding: This research was funded by the National Natural Science Foundation of China (Grant No. 52176101).

Data Availability Statement: Data are contained within the article.

Conflicts of Interest: The authors declare no conflicts of interest.

References

1. Baxter, L.L.; DeSollar, R.W. A mechanistic description of ash deposition during pulverized coal combustion: Predictions compared with observations. *Fuel* **1993**, *72*, 1411–1418. [CrossRef]
2. Wang, X.; Guo, W.; Cheng, Y.; Zheng, X. Understanding the centripetal effect and evacuation efficiency of evacuation assistants: Using the extended dynamic communication field model. *Saf. Sci.* **2015**, *74*, 150–159. [CrossRef]
3. Hupa, M. Ash-Related Issues in Fluidized-Bed Combustion of Biomasses: Recent Research Highlights. *Energy Fuels* **2012**, *26*, 4–14. [CrossRef]
4. Kleinhans, U.; Wieland, C.; Frandsen, F.J.; Spliethoff, H. Ash formation and deposition in coal and biomass fired combustion systems: Progress and challenges in the field of ash particle sticking and rebound behavior. *Prog. Energy Combust. Sci.* **2018**, *68*, 65–168. [CrossRef]
5. Li, M.-J.; Tang, S.-Z.; Wang, F.-l.; Zhao, Q.-X.; Tao, W.-Q. Gas-side fouling, erosion and corrosion of heat exchangers for middle/low temperature waste heat utilization: A review on simulation and experiment. *Appl. Therm. Eng.* **2017**, *126*, 737–761. [CrossRef]
6. Shi, H.; Wu, Y.; Zhang, M.; Zhang, Y.; Lyu, J. Ash deposition of Zhundong coal in a 350 MW pulverized coal furnace: Influence of sulfation. *Fuel* **2020**, *260*, 116317. [CrossRef]
7. Long, X.; Li, J.; Wang, H.; Liang, Y.; Lu, X.; Zhang, D. The morphological and mineralogical characteristics and thermal conductivity of ash deposits in a 220 MW CFBB firing Zhundong lignite. *Energy* **2023**, *263*, 125842. [CrossRef]
8. Cai, Y.; Tay, K.; Zheng, Z.; Yang, W.; Wang, H.; Zeng, G.; Li, Z.; Keng Boon, S.; Subbaiah, P. Modeling of ash formation and deposition processes in coal and biomass fired boilers: A comprehensive review. *Appl. Energy* **2018**, *230*, 1447–1544. [CrossRef]
9. Mavridou, S.G.; Bouris, D.G. Numerical evaluation of a heat exchanger with inline tubes of different size for reduced fouling rates. *Int. J. Heat Mass Transf.* **2012**, *55*, 5185–5195. [CrossRef]

10. García Pérez, M.; Vakkilainen, E.; Hyppänen, T. Unsteady CFD analysis of kraft recovery boiler fly-ash trajectories, sticking efficiencies and deposition rates with a mechanistic particle rebound-stick model. *Fuel* **2016**, *181*, 408–420. [CrossRef]
11. Mueller, C.; Selenius, M.; Theis, M.; Skrifvars, B.-J.; Backman, R.; Hupa, M.; Tran, H. Deposition behaviour of molten alkali-rich fly ashes—Development of a submodel for CFD applications. *Proc. Combust. Inst.* **2005**, *30*, 2991–2998. [CrossRef]
12. Yang, X.; Ingham, D.; Ma, L.; Zhou, H.; Pourkashanian, M. Understanding the ash deposition formation in Zhundong lignite combustion through dynamic CFD modelling analysis. *Fuel* **2017**, *194*, 533–543. [CrossRef]
13. Walsh, P.M.; Sayre, A.N.; Loehden, D.O.; Monroe, L.S.; Beér, J.M.; Sarofim, A.F. Deposition of bituminous coal ash on an isolated heat exchanger tube: Effects of coal properties on deposit growth. *Prog. Energy Combust. Sci.* **1990**, *16*, 327–345. [CrossRef]
14. Kleinhans, U.; Wieland, C.; Babat, S.; Scheffknecht, G.; Spliethoff, H. Ash particle sticking and rebound behavior: A mechanistic explanation and modeling approach. *Proc. Combust. Inst.* **2017**, *36*, 2341–2350. [CrossRef]
15. Kær, S.K. *Numerical Investigation of Ash Deposition in Straw-Fired Boilers*; Institut for Energiteknik, Aalborg Universitet: Aalborg, Denmark, 2001.
16. García Pérez, M.; Vakkilainen, E. A comparison of turbulence models and two and three dimensional meshes for unsteady CFD ash deposition tools. *Fuel* **2019**, *237*, 806–811. [CrossRef]
17. Balakrishnan, S.; Nagarajan, R.; Karthick, K. Mechanistic modeling, numerical simulation and validation of slag-layer growth in a coal-fired boiler. *Energy* **2015**, *81*, 462–470. [CrossRef]
18. Losurdo, M.; Spliethoff, H.; Kiel, J. Ash deposition modeling using a visco-elastic approach. *Fuel* **2012**, *102*, 145–155. [CrossRef]
19. Zhou, H.; Hu, S. Numerical simulation of ash deposition behavior with a novel erosion model using dynamic mesh. *Fuel* **2021**, *286*, 119482. [CrossRef]
20. Weber, R.; Poyraz, Y.; Beckmann, A.M.; Brinker, S. Combustion of biomass in jet flames. *Proc. Combust. Inst.* **2015**, *35*, 2749–2758. [CrossRef]
21. Tomeczek, J.; Wacławiak, K. Two-dimensional modelling of deposits formation on platen superheaters in pulverized coal boilers. *Fuel* **2009**, *88*, 1466–1471. [CrossRef]
22. Tomeczek, J.; Palugniok, H.; Ochman, J. Modelling of deposits formation on heating tubes in pulverized coal boilers. *Fuel* **2004**, *83*, 213–221. [CrossRef]
23. Garba, M.U.; Ingham, D.B.; Ma, L.; Porter, R.T.J.; Pourkashnian, M.; Tan, H.; Williams, A. Prediction of Potassium Chloride Sulfation and Its Effect on Deposition in Biomass-Fired Boilers. *Energy Fuels* **2012**, *26*, 6501–6508. [CrossRef]
24. Liang, Y.; Li, J.; Long, X.; Lu, X.; Zhang, D. A numerical simulation study of ash deposition in a circulating fluidized bed during Zhundong lignite combustion. *Fuel* **2023**, *333*, 126501. [CrossRef]
25. Li, J.; Du, W.; Cheng, L. Numerical simulation and experiment of gas-solid two phase flow and ash deposition on a novel heat transfer surface. *Appl. Therm. Eng.* **2017**, *113*, 1033–1046. [CrossRef]
26. Han, H.; He, Y.-L.; Tao, W.-Q.; Li, Y.-S. A parameter study of tube bundle heat exchangers for fouling rate reduction. *Int. J. Heat Mass Transf.* **2014**, *72*, 210–221. [CrossRef]
27. Zheng, Z.; Yang, W.; Cai, Y.; Wang, Q.; Zeng, G. Dynamic simulation on ash deposition and heat transfer behavior on a staggered tube bundle under high-temperature conditions. *Energy* **2020**, *190*, 116390. [CrossRef]
28. García Pérez, M.; Vakkilainen, E.; Hyppänen, T. The contribution of differently-sized ash particles to the fouling trends of a pilot-scale coal-fired combustor with an ash deposition CFD model. *Fuel* **2017**, *189*, 120–130. [CrossRef]
29. Mu, L.; Miao, H.; Zhao, C.; Zhai, Z.; Shang, Y.; Yin, H. Dynamic CFD modeling evaluation of ash deposition behavior and morphology evolution with different tube arrangements. *Powder Technol.* **2021**, *379*, 279–295. [CrossRef]
30. Liu, Z.; Li, J.; Wang, Q.; Lu, X.; Zhang, Y.; Zhu, M.; Zhang, Z.; Zhang, D. An experimental investigation into mineral transformation, particle agglomeration and ash deposition during combustion of Zhundong lignite in a laboratory-scale circulating fluidized bed. *Fuel* **2019**, *243*, 458–468. [CrossRef]
31. Liu, Z.; Li, J.; Zhu, M.; Wang, Q.; Lu, X.; Zhang, Y.; Zhang, Z.; Zhang, D. Morphological and Mineralogical Characterization of Ash Deposits during Circulating Fluidized Bed Combustion of Zhundong Lignite. *Energy Fuels* **2019**, *33*, 2122–2132. [CrossRef]
32. Kantak, A.A.; Galvin, J.E.; Wildemuth, D.J.; Davis, R.H. Low-velocity collisions of particles with a dry or wet wall. *Microgravity Sci. Technol.* **2005**, *17*, 18–25. [CrossRef]
33. Cheng, R.K.; Schefer, R.W.; Talbot, L.; Willis, D.R. Thermophoresis of particles in a heated boundary layer. *J. Fluid Mech.* **1980**, *101*, 737–758. [CrossRef]
34. Jokiniemi, J.K.; Pyykönen, J.; Lyyränen, J.; Mikkanen, P.; Kauppinen, E.I. Modelling Ash Deposition during the Combustion of Low Grade Fuels. In *Applications of Advanced Technology to Ash-Related Problems in Boilers*; Baxter, L., DeSollar, R., Eds.; Springer: Boston, MA, USA, 1996; pp. 591–615. [CrossRef]
35. Brink, A.; Lindberg, D.; Hupa, M.; de Tejada, M.E.; Paneru, M.; Maier, J.; Scheffknecht, G.; Pranzitelli, A.; Pourkashanian, M. A temperature-history based model for the sticking probability of impacting pulverized coal ash particles. *Fuel Process. Technol.* **2016**, *141*, 210–215. [CrossRef]
36. Venturini, P.; Borello, D.; Hanjalić, K.; Rispoli, F. Modelling of particles deposition in an environment relevant to solid fuel boilers. *Appl. Therm. Eng.* **2012**, *49*, 131–138. [CrossRef]
37. Browning, G.J.; Bryant, G.W.; Hurst, H.J.; Lucas, J.A.; Wall, T.F. An Empirical Method for the Prediction of Coal Ash Slag Viscosity. *Energy Fuels* **2003**, *17*, 731–737. [CrossRef]

38. Ji, J.; Cheng, L.; Nie, L.; Li, L.; Wei, Y. Sodium transformation simulation with a 2-D CFD model during circulating fluidized bed combustion. *Fuel* **2020**, *267*, 117175. [CrossRef]
39. Zhou, H.; Zhang, K.; Li, Y.; Zhang, J.; Zhou, M. Simulation of ash deposition in different furnace temperature with a 2D dynamic mesh model. *J. Energy Inst.* **2019**, *92*, 1743–1756. [CrossRef]
40. Liu, Z.; Li, J.; Zhu, M.; Wang, F.; Lu, X.; Zhang, Z.; Zhang, D. Experimental Investigation into Ash Deposition and Na Migration Characteristics during Combustion of High Sodium Zhundong Lignite in a Circulating Fluidized Bed Operating at Low Temperatures. *Energy Fuels* **2020**, *34*, 188–198. [CrossRef]
41. Wacławiak, K.; Kalisz, S. A practical numerical approach for prediction of particulate fouling in PC boilers. *Fuel* **2012**, *97*, 38–48. [CrossRef]
42. Lee, B.-H.; Hwang, M.-Y.; Seon, C.-Y.; Jeon, C.-H. Numerical prediction of characteristics of ash deposition in heavy fuel oil heat recovery steam generator. *J. Mech. Sci. Technol.* **2014**, *28*, 2889–2900. [CrossRef]
43. Kær, S.K.; Rosendahl, L.A.; Baxter, L.L. Towards a CFD-based mechanistic deposit formation model for straw-fired boilers. *Fuel* **2006**, *85*, 833–848. [CrossRef]
44. Zhou, H.; Zhou, B.; Li, L.; Zhang, H. Experimental Measurement of the Effective Thermal Conductivity of Ash Deposit for High Sodium Coal (Zhun Dong Coal) in a 300 KW Test Furnace. *Energy Fuels* **2013**, *27*, 7008–7022. [CrossRef]